

DEBONDING MODELLING OF INDENTATION LOADED FIBRE METAL LAMINATES

Tuomas Pärnänen^{*}, Jarno Jokinen[†], Mikko Kanerva[†], Olli Saarela[†]

^{*}Department of Applied Mechanics
Aalto University School of Engineering
P.O. Box 4300, 00076 Espoo, Finland
tuomas.parnanen@aalto.fi

[†]Department of Applied Mechanics
Aalto University School of Engineering
P.O. Box 4300, 00076 Espoo, Finland
jarno.jokinen@aalto.fi
mikko.kanerva@aalto.fi
olli.saarela@aalto.fi

Key words: debonding, indentation, FEM, fibre metal laminates

Summary: *The mechanics of debonding in a stainless steel based fibre metal laminate (type 2/1) during indentation loading was studied by means of finite element analysis. The debonding phenomenon was limited to occur between the lower stainless steel sheet and the rest of the laminate. First, the debonding was studied by simulating areal pre-cracks of different size and the strain energy release rates were monitored at the pre-crack tip during the indentation by using the virtual crack closure technique. Second, the debonding initiation and propagation were simulated by means of cohesive zone modelling. The results showed full dominance of the shearing fracture mode II for debonding during the loading step of the indentation. However, debonding propagation during the unloading step was shown to occur under the dominance of the opening fracture mode I.*

1 INTRODUCTION

Fibre metal laminates (FMLs) represent a hybrid laminate concept involving thin metal sheets and fibre reinforced plastic layers. FMLs were originally developed for aeronautical engineering applications to possess high fatigue tolerance [1]. Later on, the concept was found to hold high resistance against impact loading [2]. The high impact resistance of FMLs has been explained by the strain rate hardening of the constituent materials, as well as by various failure modes provided by the laminated structure [3-4]. The strong failure modes, i.e. fibre failure, metal plastic deformation and metal cracking, have received the majority of the research interest due to their dominant effect on laminate energy absorption. The weak failure modes, i.e. metal-composite debonding, composite delamination and matrix cracking may, however, adapt the failure process to lead to premature laminate failure due to the intensified presence of a strong failure mode.

The shear forces caused by impact and indentation loadings result in out-of-plane shear stresses in panels. In layered structures, such as composites or FMLs, this promotes

delamination initiation and progress at the layer interfaces by fracture mode II. However, our previous study on the impact response of stainless steel FMLs verified the involvement of peeling forces (fracture mode I) in the debonding process at the interface between the lower steel sheet and the rest of the laminate [5]. The peeling force participation was explained to occur during the unloading part of the impact event as a result of the dissimilar load responses of steel and fibre reinforced plastics (elastic-plastic vs. linear-elastic). Laliberté [6] also discussed in his study of low-velocity impacts on FMLs that shear stresses are responsible for delamination onset but plastically deforming metal sheets lead to opening loads during the rebound phase of the impact event. The debonding between metal sheets and fibre reinforced plastics has also been studied by Airoidi [7] who simulated the debonding of FMLs under indentation loading by cohesive element based finite element simulation. The debonding was modelled by using a series of interfacial strengths for mode I and II failure initiation. It was concluded that debonding occurred at the interface between the upper metal sheet and fibre reinforced plastic by mode II during the loading step. Depending on the material properties of cohesive elements, debonding also occurred in certain cases at the interface between the lower metal sheet and the fibre reinforced plastic during the unloading step by mode I.

This paper focuses on studying the mechanics of a debonding process in FMLs by means of finite element analysis. Particularly, the importance of fracture mode I on debonding is studied. A simplified impact event, i.e. quasi-static indentation, is used for loading the modelled FML panel. The debonding phenomenon along the interface between the lower metal sheet and the rest of the laminate is our focus. The virtual crack closure technique and cohesive zone modelling are used for simulating the debonding process. Additionally, the experimental background is described for clarity in the beginning of the study.

2 EXPERIMENTAL BACKGROUND

2.1 Laminate constituents, lay-up and preparation

The laminate being studied consisted of two AISI 304L stainless steel sheets ($t = 0.6$ mm) as outer surfaces and four layers of M21/T700GC carbon fibre epoxy UD layers [0/90/90/0] bonded in the middle using two FM300NK epoxy adhesive films (Fig. 1). The steel rolling direction corresponded with the fibre 0°-direction. The as-received steel sheets were machined to meet the final specimen size of 110 x 110 mm² prior to the cleaning and lay-up procedures. The specimens were cured in an autoclave (177 °C and 2 bar). Detailed information about the manufacturing process can be found in [5].

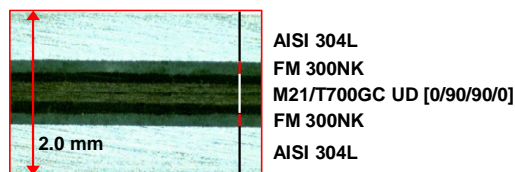


Figure 1: The cross-section of the FML.

2.2 Impact and indentation testing

Drop-weight impact loading (10 J energy, 6261 g impactor mass) was selected as an experimental reference for the modelling. A square-shaped test specimen (110 x 110 mm²) was clamped between two steel fixtures with an 80 mm diameter circular test area (Fig. 2).

An impactor with a hemispherical head (15.9 mm diameter) was used. The contact force was measured by using a load washer (20 kN) located above the impactor head. The displacement of the impactor was determined by numerically integrating the measured contact force – time curve after the impact event. Further details for the drop-weight impact testing can be found in [5].

A quasi-static (indentation) reference for the modelling was performed using a servo-hydraulic tester with the impactor and steel fixtures (Fig. 2). The displacement rate during the testing was 2 mm/min. The force limit for an indentation test was set to correspond with the maximum contact force observed during the 10 J impact event (4.9 kN). The contact force of the impactor head was measured using the load cell of the tester (100 kN) and the displacement with an auxiliary LVDT mounted on the impactor support fixture (Fig. 2).

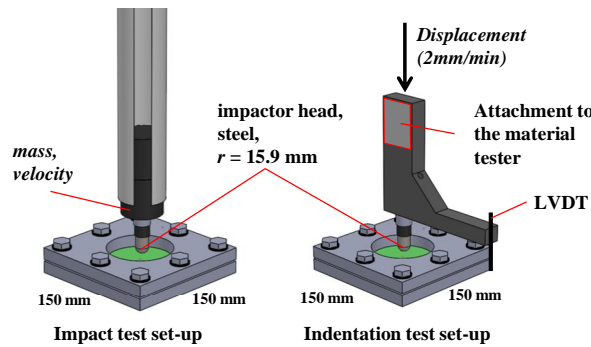


Figure 2: The test set-up for the impact and indentation testing.

2.3 Post-loading deflection profiles

The post-loading deflection profiles of the specimens were measured from the surface of the bottom-side steel and along a line crossing the impact point in the laminate 90°-direction. The deflection profiles were measured using a laser displacement sensor (Keyence, Japan) with 4 points/mm spatial resolution.

3 FINITE ELEMENT ANALYSIS

3.1 FML Finite element model

The finite element model was built using Abaqus (standard) v6.14 in a 3D deformable frame. The contactor head was modelled as a linear-elastic material using 10-node quadratic tetrahedron elements (C3D10). The FML specimen was modelled using 8-node linear brick elements (C3D8R). The carbon fibre epoxy layers and the adhesive layers utilized linear-elastic material models, whereas the elastic-plastic response of the steel layers was modelled by applying the Johnson-Cook hardening model. The material parameters for the constituent layers are listed in Table 1. The material parameters for the Johnson-Cook model ($A = 250$ MPa, $B = 1350$ MPa and $n = 0.7$) were fitted along with the in-house tensile test results for 304L tested according to ASTM E8–09. The constituent models did not include any failure criteria for in-plane loading. The element mesh of each layer had two elements in the thickness direction. The area for the debonding study ($R < 10$ mm) was modelled using a sweep algorithm, which resulted in 44 elements along the periphery. The rest of the panel area was meshed using an approximate global element size of 2 mm. Finally, each layer included 8200 elements. The overview of the mesh is shown in Fig. 3.

Property	Carbon-epoxy UD M21/T700GC	Steel AISI 304L	Adhesive film FM300NK	Steel Contactor head
t [mm]	0.127	0.6	0.15	
E [GPa]	124.9 (E_1) ^a 7.2 (E_2) ^a 7.2 (E_3) ^a	197.5 ^c	2.8 ^f	210
ν [-]	0.31 (ν_{12}) ^a 0.31 (ν_{13}) 0.38 (ν_{23})	0.264 ^d	0.4 ^f	0.3
G [GPa]	4.0 (G_{12}) ^a 4.0 (G_{13}) 2.6 (G_{23})			
α [10^{-6} m/(m°C)]	0.22 (α_1) ^b 40.7 (α_2) ^b 40.7 (α_3) ^b	16.9 ^e	48.6 ^g	

^a In-house testing (ASTM D3039-00)

^b Ref [8]

^c In-house testing (ASTM E111-97)

^d In-house testing (ASTM E132-04)

^e Ref [9]

^f Ref [10] (FM300U)

^g Ref [11] (FM300U)

Table 1: The constituent material properties for the bulk materials.

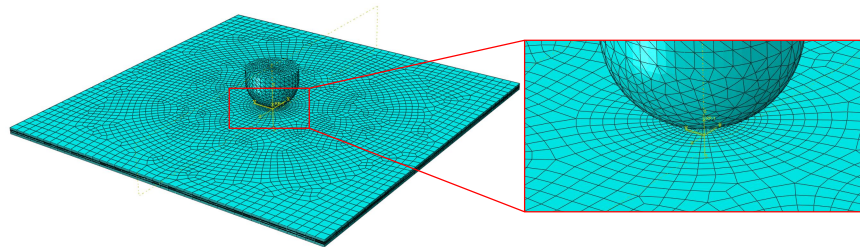


Figure 3: The finite element model.

The contact between the impactor head and the FML was modelled as a general contact with frictionless behaviour. A thermal load was implemented to the specimen prior to the indentation loading in order to account for curing residual stresses (curing at 177 °C and testing at 22 °C). The displacement of the specimen's upper and lower surfaces outside the test area ($r = 80$ mm) was prevented in the out-of-plane direction after the thermal load. The in-plane translations were fixed at selected points to allow free in-plane translation of the FML near the edges of the circular test area. The loading by the impactor head was modelled using enforced displacement. The maximum displacement of the impactor was set to meet the maximum displacement during the 10 J impact event ($u_{\max} = 3.7$ mm). The translations of the impactor top surface in the two other directions were prevented. After the loading, an unloading step was followed during which the impactor was returned to the initial position.

Two separate modelling techniques were used for monitoring the debonding phenomenon between the lower adhesive film and the lower steel sheet: (1) the virtual crack closure technique and (2) cohesive zone modelling. The modelling details are given in the following sections. The rest of the layer interfaces were rigidly connected using tie constraints.

3.2 Determination of strain energy release rates

The virtual crack closure technique (VCCT) is a linear-elastic fracture mechanics based method suitable for modelling delamination or debonding propagation. The theory for VCCT can be found in [12]. The method requires a pre-crack prior to crack propagation. In the present study, VCCT was applied purely for monitoring strain energy release rate values at the edges of the modelled pre-cracked areas. Therefore, the critical strain energy release rates ($G_{IC}, G_{IIC}, G_{IIIC}$) were set to possess considerably higher values when compared to a real structure in order to prevent any crack growth. The pre-cracks for the simulations were modelled as circle-shaped areas with various radiuses (Fig. 4 and Table 2).

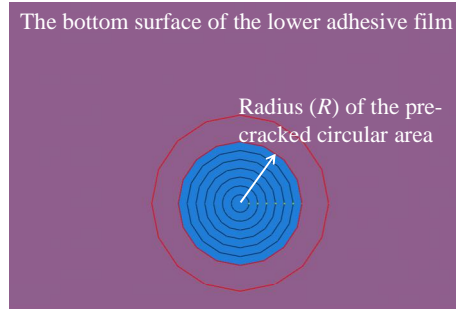


Figure 4: Example of pre-crack selection for VCCT modelling (VCCT-R7mm). The origin for the circular shaped pre-crack is located at the specimen contact point.

Model	Pre-crack radius [mm]
VCCT-R1mm	1
VCCT-R2mm	2
VCCT-R3mm	3
VCCT-R4mm	4
VCCT-R7mm	7

Table 2: Pre-crack radiuses for the VCCT simulations.

3.3 Debonding initiation and propagation model

Cohesive zone modelling was used for simulating debonding initiation and propagation in the present study. The failure was modelled by using a bilinear cohesive zone law in which failure initiation obeyed a quadratic nominal stress criterion and damage evolution followed a power law criterion (see Fig. 5). Three-dimensional 8-node cohesive elements (COH3D8) were used for the modelling. The area for the cohesive zone modelling was a circular domain with a radius of $R = 7$ mm located around the specimen contact point (Fig. 6). The rest of the interface ($R > 7$ mm) between the lower adhesive film and the steel sheet was connected by a tie constraint. The material parameters for the cohesive zone modelling are listed in Table 3. The modelling included three sets of values for the nominal ultimate stresses and the ratio between the values followed the ratio between the critical strain energy release rates (i.e. $t_n^0/t_s^0 = G_{IC}/G_{IIC}$).

Model	t_n^0 [MPa]	t_s^0 [MPa]	t_t^0 [MPa]	K_{nn} [N/m ³]	K_{ss} [N/m ³]	K_{tt} [N/m ³]	G_{IC} [J/m ²]	G_{IIC} [J/m ²]	G_{IIIC} [J/m ²]
Cohesion-25/50	25	50	50	5E+14	5E+14	5E+14	1750 ^a	3500 ^a	3500
Cohesion-37.5/75	37.5	75	75	5E+14	5E+14	5E+14	1750 ^a	3500 ^a	3500
Cohesion-50/100	50	100	100	5E+14	5E+14	5E+14	1750 ^a	3500 ^a	3500

^a Ref [13] (FM300K)

Table 3: Material parameters applied in the cohesive zone models of the FML.

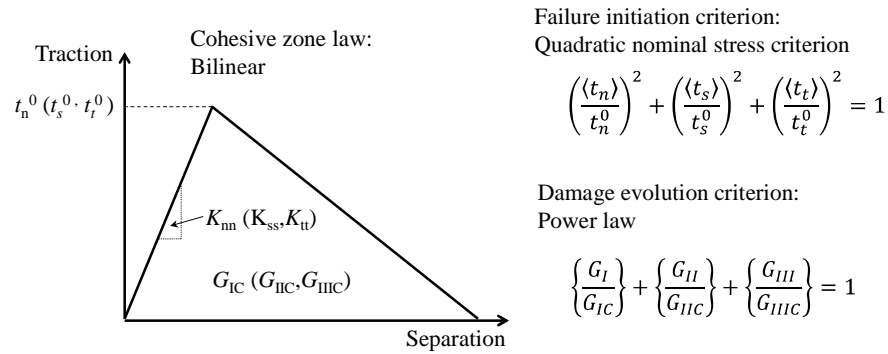


Figure 5: Cohesive zone law and criteria used in the FML modelling of this study.

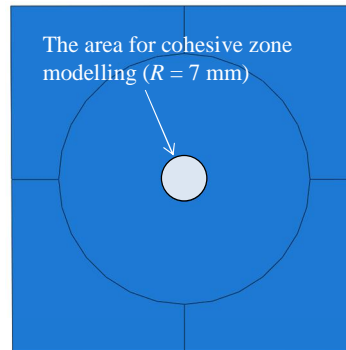


Figure 6: Area for cohesive zone elements in the FML models of this study.

4 RESULTS

4.1 Global indentation response

As a representative example of the current simulations, Fig. 7 illustrates the debonding response of the FML model after the impactor has been withdrawn. The lower steel sheet has separated from the laminate around the contact point.

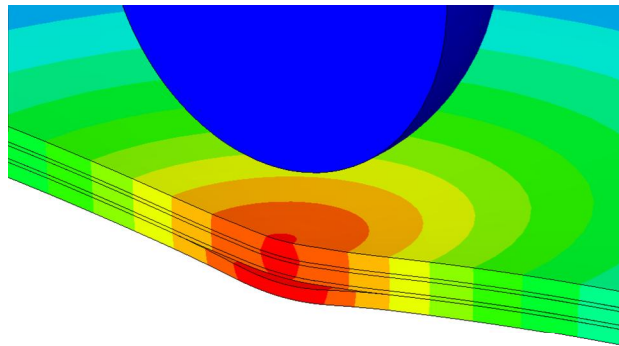


Figure 7: Representative example of the specimen response after the indentation event (Cohesion-37.5/75).

Fig. 8 shows the contact force – displacement response for the extremes of the VCCT and cohesive zone models (VCCT-R1mm, VCCT-R7mm, Cohesion-25/50 and Cohesion-50/100). The simulated behaviour was between the experimental impact and quasi-static indentation curves. The most remarkable difference between the models occurred at the final part of the unloading where the slopes of the curves differed.

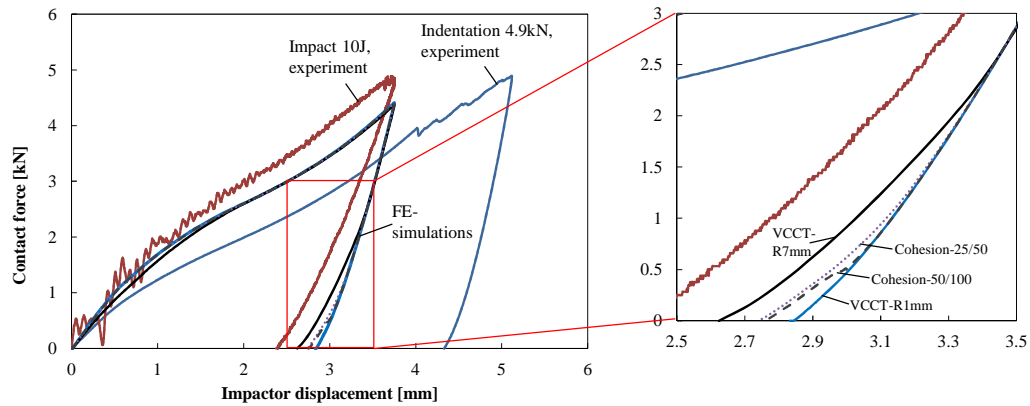


Figure 8: The contact force – impactor displacement curves for the extremes of the VCCT and cohesion zone models, i.e. VCCT-1mm, VCCT-7mm, Cohesion-25/50 and Cohesion-50/100.

The deflection profiles for the extreme VCCT and cohesive zone models can be seen in Fig. 9. The VCCT model with the largest pre-crack (VCCT-7mm) resulted in the highest maximum deflection. Analogous to the contact force – displacement curves, the cohesive zone model behaved according to the VCCT model with a moderate pre-crack size.

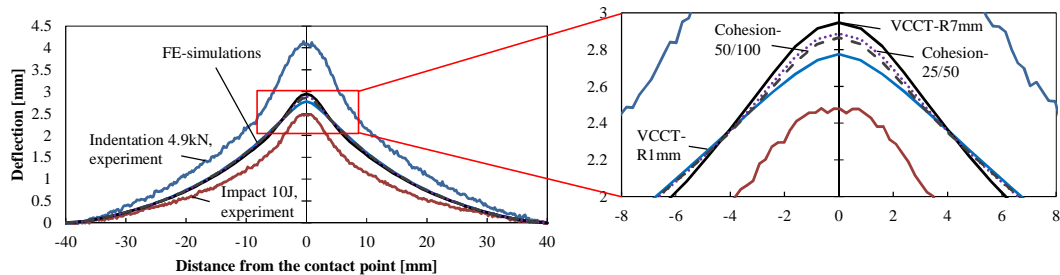


Figure 9: The post-loading deflection profiles for the extremes of VCCT and cohesion zone models, i.e. VCCT-1mm, VCCT-7mm, Cohesion-25/50 and Cohesion-50/100.

4.2 Strain energy release rates (SERR) at the pre-crack tip

The FML debonding phenomenon was approximated using the VCCT models and various-sized circular pre-cracks located at the interface between the lower adhesive film and the lower steel sheet. Figs. 10 and 11 summarize the shearing fracture (mode II) and opening fracture (mode I) SERR response during the simulated loading. The results are averages of the nodal SERR values on the pre-crack periphery. The results suggest full mode II dominance during the loading step since the mode I values remain zero. The growth of mode II SERR (per impactor displacement) is highest for 1 mm and 2 mm pre-crack radiuses in the beginning of the impact. The maximum SERR value is reached with a 2 mm pre-crack radius. During the unloading step (impactor withdraw), the mode II SERR values decrease. Finally, as the impactor-FML contact is lost, approximately constant SERR is reached (250 J/m^2). The response of the model with a 1 mm pre-crack radius was different - the SERR value decreases fast and reaches zero before the unloading step.

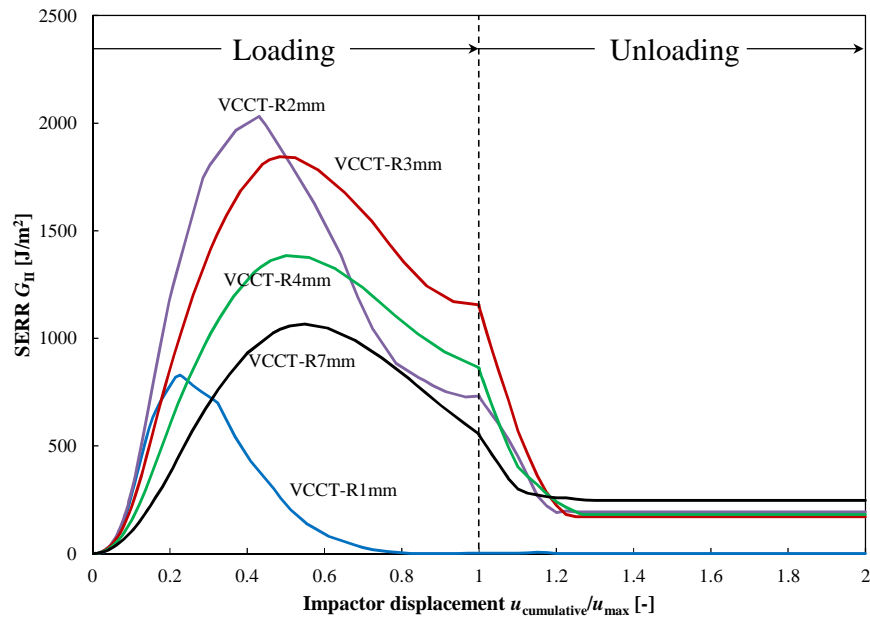


Figure 10: The average shearing mode II strain energy release rates at the pre-crack tip for various pre-crack radiuses modelled with VCCT.

Despite the constant mode II SERR finally reached (250 J/m^2), the debonding during impactor withdrawal is clearly dominated by the opening (mode I) crack tip loading (Fig. 11). The highest mode I SERR value is obtained with a 2 mm pre-crack radius. The increase in the pre-crack radius seemed to reduce the maximum mode I SERR. It should be noted that the mode I SERR exceeds the critical SERR ($G_{IC} = 1750 \text{ J/m}^2$) approximated for the steel-epoxy interface (models with 1 mm, 2 mm and 3 mm pre-crack radiuses).

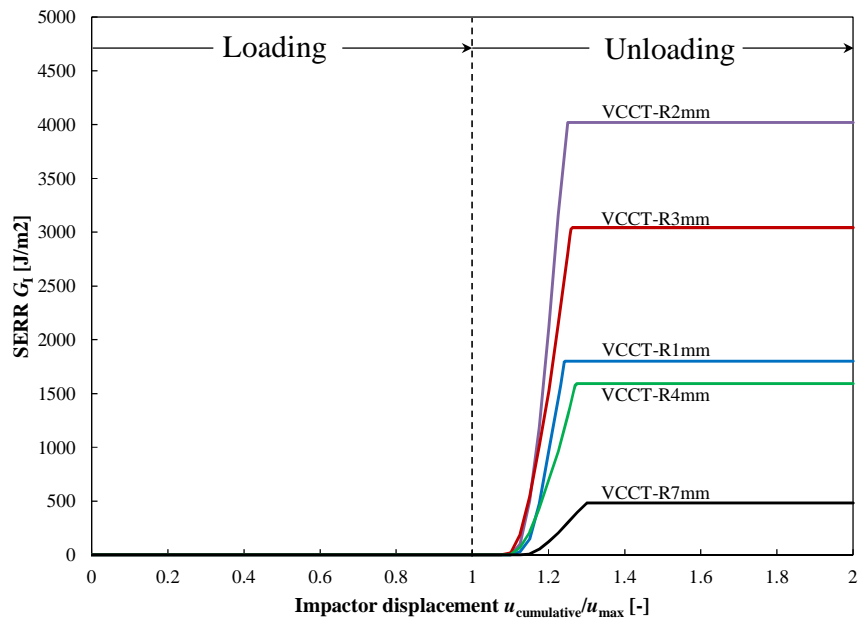


Figure 11: The average opening mode I strain energy release rates at the pre-crack tip for various pre-crack radiuses modelled with VCCT.

4.3 Simulated debonding initiation and propagation

The results of debonding initiation and propagation obtained with the cohesive zone model are summarized in Fig. 12. The model with lowest nominal ultimate stresses (Cohesion-25/50) suggested damage initiation at the early stage of the loading (7% loading). The damage initiated at an approximate distance of 1.2 mm from the specimen contact point and in three different locations (Fig. 12a). The debonding progressed forming two crescent-shaped debonding areas around the contact point. As the loading increased, the debonding propagated and formed a single circle-shaped debonding area with a maximum radius of 2.9 mm (the end of the loading step). The size and the shape of debonding did not markedly change at a loading range from 45% to 100% (loading step). It should be noted that the centre (the specimen contact point) had a small area without debonding. However, during the early stage of impactor withdrawal, this small area debonded. The radius of the total debonding area resumed increasing as $\approx 15\%$ of the unloading step (impactor withdrawal) was completed. After that, the debonding propagated until the contact between the FML and the impactor was lost as $\approx 27\%$ of the unloading step was completed. The final radius of the debonding area was $R_{\max} = 4.8$ mm.

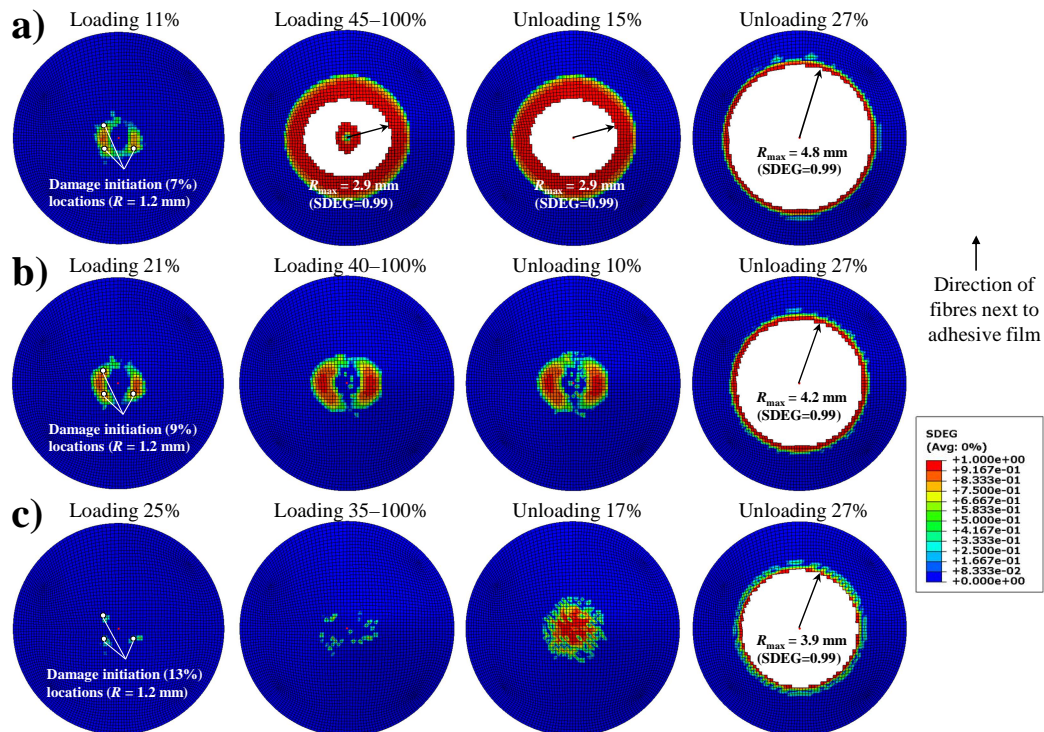


Figure 12: The debonding evolution of a) Cohesion-25/50, b) Cohesion-37.5/75 and c) Cohesion-50/100 models. SDEG represents the state of the damage evolution criterion (SDEG = 0 no damage, SDEG = 1 full damage). The elements exceeding SDEG = 0.99 are removed (white area).

The model with increased nominal ultimate stresses (Cohesion-37.5/75) showed debonding initiation to occur at the same locations as the first model, even though a higher contact force (9% load level) was needed (Fig. 12b). The shape of the debonding represented two crescent-shaped areas to the end of the loading step. After $\approx 10\%$ of the unloading step (impactor withdrawal), the debonding begun to propagate fast and formed a circular-shaped debonding area – the maximum radius of the debonding area was $R_{\max} = 4.2$ mm.

The behaviour of the model with the highest nominal ultimate stresses (Cohesion-50/100) showed debonding initiation to occur at the same locations as the previous models: after $\approx 13\%$ of loading (Fig. 12c). However, any apparent debonding formation did not arise during the loading step. Remarkably fast debonding emerged after $\approx 17\%$ of the unloading step (impactor withdrawal). The debonding formed a circular-shaped debonding area and continued to propagate until the contact between the FML and the impactor was lost. The maximum radius of the debonding area was $R_{\max} = 3.9$ mm.

5 DISCUSSION

The stainless steel in the modelled FML experiences plastic deformation during loading. The simulation using VCCT violates the initial assumption of linear-elastic fracture mechanics, which presumably introduces an undefined error to the strain energy release rate values. However, our results using the models with VCCT express the dominance of fracture loading modes during the simulated indentation (Fig. 13). According to the results, the “loading step” is fully dominated by mode II. During impactor withdrawal, the mode II SERR values decrease. While the “unloading step” continues, mode I loading takes place and increases. After the entire loading event, an amount of mode II SERR exists but the pre-crack tip is clearly mode I SERR dominated.

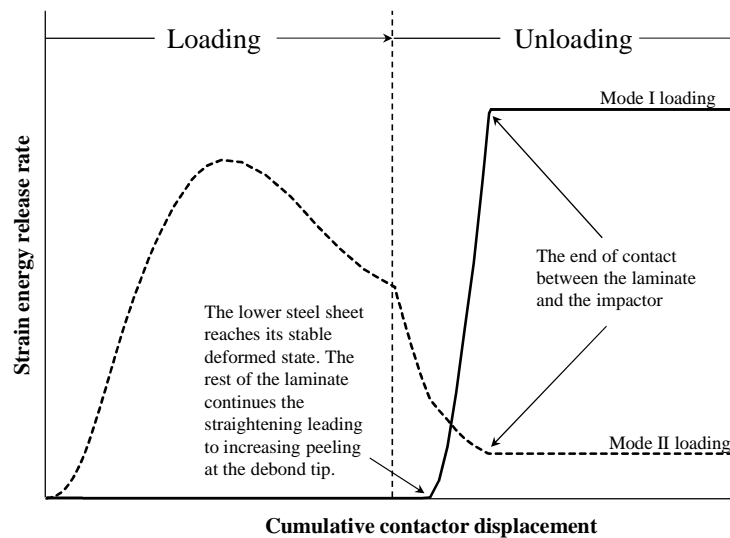


Figure 13: A schematic presentation of mode I and mode II loading at debond/pre-crack tip during indentation loading.

The FML models with cohesive elements provided information about debonding initiation and propagation. The analysis lacked the possibility to monitor individual SERR components. Debonding propagation using the FML models with cohesive elements corresponded with the FML models with VCCT as follows: as the SERR values (either mode I or mode II) increased at the pre-defined crack-tip (VCCT), debonding propagated in the cohesive elements. Thus, our finite element analysis verifies that debonding during indentation by an impactor is initiated by mode II crack-tip loading, and debonding (or propagation) during impactor withdrawal is driven by mode I crack-tip loading.

The results of this study support the experimental evidence about debonding mechanics during impactor withdrawal for low-velocity impacts discussed in our previous study [5]. In its simplicity, an FML specimen first releases the elastic strain energy gained during the “loading step” (Fig. 13). After the lower stainless steel sheet (elastic-plastic response) has released all its elastic strain energy, it sustains the deformed shape. Simultaneously, the rest of the FML specimen (linear-elastic composite layers) will continue the straightening towards to the initial flat state. However, the lower stainless steel sheet constraints the straightening and the crack-tip of the debond experiences mode I loading. After a force balance is reached, a residual mode I SERR remains.

In a real FML panel, layer separation may also occur at the interfaces between the composite layers, as well as at the interface between the upper metal sheet and the rest of the FML panel. Moreover, the intensity of the overall debonding is presumably dependent on the fibre and metal cracking. The analysis in the present paper focused on a low magnitude of impact or indentation loading when these failures are likely lacking. The full focus on a single failure mode, i.e. on debonding at a single layer interface also led to stiffer behaviour when compared to the indentation experiment. Due to these considerations, our future simulation work shall be extended to take into account other failure modes and debonding/delamination locations to study the mechanics of the FML failure process further.

6 CONCLUSIONS

The research work presented here focused on describing a debonding phenomenon in fibre metal laminates (FMLs) due to indentation loading. The debonding along the interface between a lower stainless steel sheet and the rest of the FML was analysed. The simulated results indicated a division between the loading modes at the debonding crack-tip:

(1) There is pure shearing (mode II) crack-tip loading during the first stages of indentation by a spherical impactor.

(2) The opening (mode I) crack-tip loading increases and finally dominates during the impactor withdrawal stage of indentation.

Additionally, it was observed that the progression of debonding affects the contact force – impactor displacement response (slope of the curve) at the end of the unloading phase. Respectively, extensive debonding increases the maximum residual (plastic) deformation of the panel’s outer surface.

ACKNOWLEDGEMENTS

This work was funded by the Graduate Program of Engineering Mechanics (Finland) and the W. Ahlström Research Foundation. The authors are grateful to Patria Aerostructures Oy and Outokumpu Oyj for their co-operation during the research.

REFERENCES

- [1] A. Asundi, Alta Y.N. Choi, *Fiber metal laminates: An advanced material for future aircraft*. Journal of Materials Processing Technology, 63(1–3), 384-394, 1997.
- [2] A. Vlot, E. Kroon, G. La Rocca, *Impact Response of Fiber Metal Laminates*. Key Engineering Materials, 141-143, 235-276, 1997.

- [3] L.B. Vogelesang, A. Vlot, *Development of fibre metal laminates for advanced aerospace structures*. Journal of Materials Processing Technology, 103, 1-5, 2000.
- [4] A.Vlot, M. Krull, *Impact Damage Resistance of Various Fibre Metal Laminates*. Journal de Physique IV, 7(C3), 605-616, 1997.
- [5] T. Pärnänen, M. Kanerva, E. Sarlin, O. Saarela, *Debonding and impact damage in stainless steel fibre metal laminates prior to metal fracture*. Composite Structures, 119, 777-786, 2015.
- [6] JF. Laliberté, *Investigation of Low-Velocity Impact Damage in Fibre-Metal-Laminates*. Dissertation, Carleton University, Canada, 2002.
- [7] A. Airoidi, M. Vesco, S. van der Zwaag, A. Baldi, G. Sala, *Damage in glare laminates under indentation loads: experimental and numerical results*. 17th International Conference on Composite Materials (ICCM17), Edinburgh, UK, 27-31 July, 2009.
- [8] Y. Nawab, F. Jacquemin, P. Casari, N. Boyard, Y. Borjon-Piron, V.Sobotka, *Study of variation of thermal expansion coefficients in carbon/epoxy laminated composite plates*. Composites Part B: Engineering, 50, 144-149, 2013.
- [9] Outokumpu, *Type 304, Type 304L UNS S30400, UNS S30403 The basic austenitic stainless steel, a versatile corrosion resistant material for general purpose applications*. Datasheet.
- [10] M. Kanerva, O. Saarela, *X-ray diffraction and fracture based analysis of residual stresses in stainless steel-epoxy interfaces with electropolishing and acid etching substrate treatments*. International Journal of Adhesion and Adhesives, 39, 60-67, 2012.
- [11] M. Kanerva, E. Sarlin, O. Saarela, *Variation in mode II dominated interface fracture of stainless steel-epoxy bonds. Part I: Mechanical testing*. Engineering Fracture Mechanics, 99, 147-158, 2013.
- [12] R. Krueger, *Virtual crack closure technique: History, approach, and applications*. Applied Mechanics Reviews, 57(2), 109-143, 2004.
- [13] A.J. Russell, *A Damage Tolerance Assessment of Bonded Repairs to CF-18 Composite Components Part I: Adhesive Properties*. DREP-Technical Memorandum-88-25, 1988.